Journal of Materials Chemistry C

ROYAL SOCIETY OF CHEMISTRY

PAPER

View Article Online
View Journal | View Issue

Cite this: J. Mater. Chem. C, 2022, 10, 11730

Lignin-derived porous graphene for wearable and ultrasensitive strain sensors†

Shuhong Yang,[a] Yun Ling,[a] Qian Wu,[b] Hanwen Zhang,[a] Zheng Yan,[ab] Guoliang Huang,[b] Jian Lin[b] and Caixia Wan*[a]

Received 9th March 2022,
Accepted 11th July 2022

DOI: 10.1039/d2tc00953f

rsc.li/materials-c

This study aimed to explore lignin as a naturally occurring aromatic precursor for the synthesis of LIG and further fabrication of ultrasensitive strain sensors for the detection of small deformations. One-step direct laser writing (DLW) induced high quality porous graphene, so called laser induced graphene (LIG), from kraft lignin under the conditions optimized for laser power, focus distance, and lignin loading. An electrode based on the resulting LIG was facilely fabricated by transferring LIG onto an elastomeric substrate (*i.e.*, Dragon Skin™). The novel LIG transfer was facilitated by spin coating followed by water lifting, leading to the full retention of porous graphene onto the elastomeric substrate. The strain sensor was shown to be highly sensitive to small human body motions and tiny deformations caused by vibrations. It had a working range of up to 14% strain with a gauge factor of 960 and showed high stability as evidenced by repetitive signals over 10 000 cycles at 4% strain. The sensor was also successfully demonstrated for detecting human speaking, breath, seismocardiography (SCG), and movement of pulse and eye. Overall, the lignin-derived LIG can serve as excellent piezoresistive materials for wearable, stretchable, and ultrasensitive strain sensors with applications in human body motion monitoring and sound-related applications.

1. Introduction

Strain sensors can be used as wearable and healthcare-oriented electronics for human health monitoring. In general, there are two main categories of human body motion detections, including large scale (bending, jumping, movements of arms and legs, *etc.*) and small scale (pulse, breath, and other tiny muscle movements).[1–6] A high-performance strain sensor would require a large working range, high sensitivity, long durability, low fabrication cost, *etc.* Numerous materials, such as carbon nanotubes (CNTs),[7–9] nanoparticles,[10] graphene,[1,11] and laser-induced graphene (LIG),[12–17] have been reported for developing the high-performance strain sensor to fulfill the increasing demands for human health monitoring. However, most strain sensors have limitations in sensing. For example, a CNT-based strain sensor with PDMS as an elastomeric substrate had a low gauge factor (0.82–14) although it exhibited excellent stretchability.[8,9] Similarly, the strain sensor based on CVD-grown graphene showed high sensitivity in the detection of small-scale human motions, but it can only be stretched at 7% strain or below, with a gauge factor only up to 35.[1] A sensor configuration like sandwiched structure can significantly improve gauge factors,[18,19] but the correlation between signals and applied strains would need to be further improved. Therefore, further efforts would be needed to explore new piezoresistive materials and advance sensor fabrication techniques for developing ultrasensitive, wearable, and stretchable strain sensors at low cost.

LIG has been explored as an active material for strain sensor fabrication, as aforementioned. LIG can be facilely synthesized from various precursors using single-step direct laser writing (DLW), exhibiting excellent electrical, chemical, and mechanical properties.[14,16,20,21] More strikingly, it has intrinsic porous structures which typically cannot be achieved by traditional techniques for graphene synthesis. Such an attribute makes LIG a unique active element for strain sensor fabrication. LIG-based strain sensors particularly derived from polyimide (PI) have been reported to outperform CVD-grown graphene sensors,[22] and show high sensitivity to capture various human body motions (*e.g.*, speaking, pulse detection, and arm movements).[12,16,17,23,24] However, these sensors had limited detection strain ranges (below 1% strain) and gauge factors below 30 if the LIG-embedded PI film was used as a substrate for sensor fabrication.[12] While stretchable strain sensors can be realized by transferring PI-derived LIG onto an elastomer,

[a] Department of Biomedical, Biological, and Chemical Engineering, University of Missouri, 1406 East Rollins Street, Columbia 65211, USA. E-mail: wanca@missouri.edu; Tel: +1 573 884 7882
[b] Department of Mechanical and Aerospace Engineering, University of Missouri, 416 South 6th, Columbia 65211, USA

† Electronic supplementary information (ESI) available. See DOI: https://doi.org/10.1039/d2tc00953f

the gauge factors were still below 200 with significantly decreased sensitivity in the small strain detection. One major reason for comprised sensitivity is the drastically increased sheet resistance (>20 kΩ) associated with LIG transfer.[15] LIG synthesized from other precursors such as cellulose paper was also used to fabricate on-chip, flexible strain sensors; however, the as-prepared sensors had poor stretchability and a very low working range (0–0.3% strain) and low gauge factors (only up to 42).[25] To fully explore the potential of LIG to be an active material for strain sensors, technical barriers such as the LIG quality, sensitivity, and transferability would need to be tackled.

Among various precursors (polyimide, wood, *etc.*) explored for LIG,[25–29] lignin stands out as a unique natural precursor for graphene synthesis given its high-carbon and aromatic structures. Compared to cellulose and hemicellulose, lignin is the most favorable constituent in the lignocellulosic biomass for LIG formation. Lignin separated from the biomass, so called technical lignin, is more processable than the raw biomass like wood to form a suitable substrate for DLW and yield a higher quality of LIG. On the other hand, in pulping mills and biorefinery facilities, lignin is generated in large quantities (>100 million dry tons annually) as waste streams.[30] Therefore, upgrading lignin into graphene-based materials can add additional revenues and be of great significance to the paper and pulp and biorefinery industries. As lignin is typically recovered in a powder form from biorefinery, lignin-based films can be made using a binder such as PVA, PEO, and cellulose nanofibers (typically not contributing to LIG formation) to well suit direct laser writing.[31–33] This strategy would enable the mass production of lignin derived LIG as renewable advanced carbon materials *via* a roll-to-roll manufacturing process. Prior studies reported that lignin derived LIG has high potential in energy storage and sensing applications.[26,28,32] However, research on lignin to LIG and subsequent applications is still limited compared to PI, a synthetic polymer precursor. For strain sensing, few research studies have been performed to explore lignin derived LIG as an active material. A recent study reported a strain sensor based on lignin derived LIG/PDMS for human motion monitoring but with low sensitivity as reflected by a quite low gauge factor of 20 because of the low LIG quality.[34] Therefore, more research efforts are needed for tailoring the properties of lignin derived LIG as an excellent piezoresistive material. Further exploration of the lignin-to-LIG upgrading pathway would need to address technical barriers to both LIG and lignin-specific precursors. For example, for sensing applications, the sensor fabrication could involve LIG transfer from a lignin-based substrate (*e.g.*, film); however, carbon loss, a common issue with LIG regardless of precursors, should be mitigated. Another consideration is to obtain high quality LIG such as crystalline graphene since abundant oxygen-containing functionalities in lignin and biomass would contribute to noticeable defects in LIG. To this end, it would be very necessary to tune lasing conditions to ensure the LIG quality.

In this study, we demonstrated the feasibility to fabricate a stretchable and wearable strain sensor using lignin derived LIG. LIG was synthesized from kraft lignin by DLW and further transferred onto Dragon Skin™ for sensor fabrication. The LIG transfer was facilitated by a novel technique based on spin coating coupled with water lifting, without a noticeable modification on the 3D structure of LIG. The key parameters optimized for lasing included precursor loading, laser power, and defocus distance. The resultant LIG was characterized for microstructure and graphene domains. The fabricated strain sensor showed an ultrasensitive response to external stimuli including strains up to 14% and vibrations (5–135 Hz) with high stability. The excellent sensing performance underscored that lignin derived LIG can serve as a highly promising piezoresistive material for detecting tiny deformations induced by strains (below 6%) and vibrations.

2. Methods

2.1. LIG synthesis

A lignin-based film was prepared by mixing kraft lignin with polyvinyl alcohol (PVA). In brief, PVA (M_w = 146 000–186 000) was first dissolved at 9 wt% in deionized (DI) water by continuous stirring at 90 °C for 40 min. Kraft lignin of 0.5, 1.0, or 1.5 g was dissolved in 10 g of 2 wt% NaOH solution. Then, the kraft lignin solution was mixed with the PVA solution at 1 : 1, w/w until a clear, dark brown liquid was obtained. The liquid was cast onto a plastic Petri dish with 9 cm in diameter and dried at 35 °C in an incubator with a humidity of 25–50% for about 30 h. After drying, the film was peeled off from the Petri dish and attached to a glass slide using an adhesive tape for laser writing.

A CO_2 laser (30 W, 10.6 μm, Universal Laser Systems VLS3.50 Laser Cutter/Engraver) was used for DLW. The process was conducted under ambient conditions, with 1000 pulses per inch, 10% speed, varying *z*-axis distances from the focal plane (0.0, 1.0, 2.0, and 3.0 mm), and varying powers (20%, 30%, and 40% of the upper limit of the laser power setting). An area of 3.0 × 0.5 cm^2 on the lignin-based film was subjected to laser writing. The LIG samples were denoted as LxPy with a 2 mm *z*-axis defocus distance unless stated otherwise, where *x* stands for the initial mass loading of lignin in a film (*i.e.*, 0.5, 1.0, or 1.5 g) and *y* stands for the laser power level (*i.e.*, 20%, 30%, or 40%).

2.2. Fabrication of strain sensors

A strain sensor was fabricated by transferring LIG onto Dragon Skin™ (Dragon Skin™ 10 FAST Silicones), an elastomeric substrate. First, Dragon Skin™ was prepared by mixing two prepolymers (Part A : Part B = 1 : 1, w/w) and then coated to LIG embedded onto the lignin film using a spin coater (Model WS-650MZ-23NPPB) with a spin speed of 3000 rpm and an accelerated speed of 500 rpm s^{-1}. After spin coating, Dragon Skin™ was cured in a convection oven at 35 °C for 30 min. The Dragon Skin™-coated film was then immersed in DI water for about 10 min to facilitate the detachment of LIG from the lignin film. The LIG/Dragon Skin™ composite was then dried at

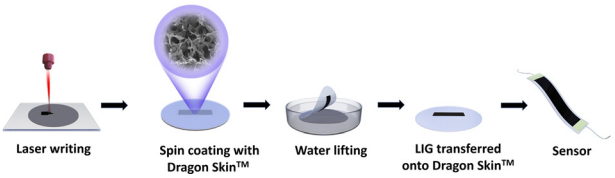

Fig. 1 Schematic diagram of strain sensor fabrication from lignin derived LIG.

35 °C in a convection oven for 20 min, cut into a dimension of 3.8 × 0.85 cm^2, and used for the sensor fabrication. The composite was further attached with two copper wires on both ends using a conductive epoxy adhesive followed by air drying. Fig. 1 illustrates the sensor fabrication from lignin derived LIG.

2.3. Characterization

LIG embedded onto a film was used for characterization, unless stated otherwise. Raman spectra were acquired on an inVia™ confocal Raman microscope at a wavelength of 633 nm. The sheet resistance (Rs) was measured using Pro-4 Four Point Resistivity Systems (Lucas Labs, Gilroy, CA). The morphology of LIG samples was examined using a scanning electron microscope (SEM, FEI Quanta 600 FEG) equipped with a Bruker Quantax 200 Silicon Drift Detector and operated at 15 kV and 100 pA. High resolution transmission electron microscopy (HRTEM) images were acquired using a JEOL-2100FFEI Tecnai G2 F30 300 kV microscope, and the LIG powder was sonicated in ethanol for 10 min and imaged. X-ray diffraction (XRD) scanning was performed for the LIG powder at 0.02° step size at a scanning rate of 12 s/0.02° using a Bruker SMART CCD system.

2.4. Sensing evaluation

Signal patterns for sensing were acquired using an LCR meter (HIOKI IM3523 LCT meter) operated at a DC voltage of 0.1 V. For strain sensing, the sensor was stretched at a varying strain at a rate of 0.2 mm min^{-1} using a motorized test stand (Mark-10 ESM30) for testing. To detect vibration, a Permanent Magnet Shaker LDS (B&K V203) was used to vibrate the sensor at a frequency of 0–135 Hz or an input voltage of 0–3 V. The invoked amplitudes of the shaker were proportional to the input voltages. At each level of frequency or input voltage, the strain was kept being vibrated for 10 s. Small-scale human motion detections were also performed, including speaking, eyeball movements, heartbeats (pulses), and breath. The sensor was attached onto the tester's eyes, throat, wrist, and belly using a biocompatible adhesive gel for signal collecting.

3. Results and discussion

3.1. Characterization of lignin derived LIG

Raman spectra reveal that all the LIG samples had three dominant peaks including D, G, and 2D peaks (Fig. S1, ESI†). Specifically, a D peak at ~1360 cm^{-1} reflects defects and bending of sp^2 carbon bonds; a G peak at ~1580 cm^{-1} arises from the first order band of all sp^2 hybridized bonds; and a 2D peak at ~2670 cm^{-1} originates from the second order zone boundary phonons.[35] High I_G/I_D and I_{2D}/I_G ratios indicate high degrees of graphitization and quality graphene, respectively. The laser power showed different effects on the films with different lignin loadings. For L0.5, the higher laser power better induced graphene (Fig. S1a, ESI†). For L1.0, 30% laser power appeared to be sufficient for inducing higher quality LIG with I_G/I_D and I_{2D}/I_G ratios of 2.7 and 0.77 (Fig. S1d and e, ESI†), respectively, indicating the formation of few-layer graphene with higher quality compared to the counterparts derived from other precursors (*e.g.*, PI, polyetherimide, wood, and cellulose paper) and even lignin reported in prior studies.[25–29] Further increasing lignin loading in the film (L1.5) did not necessarily improve the LIG quality regardless of the laser power applied (Fig. S1c, ESI†). In general, the high laser power can lead to sufficient carbonization and further graphitization.[26,29] However, the laser power, if too high, can cause detrimental effects on the LIG quality due to severe photothermal irradiation. It should be noted that PVA in the lignin-based composite film would decompose and release as gaseous products (H_2O, CO_2, *etc.*) during laser scribing rather than contributing to LIG synthesis. The Raman spectra show that the threshold of the laser power for inducing porous graphene would also be related to lignin loading in a substrate. In the case of L1.5, the laser parameter would need to be further optimized due to higher lignin loading. In consistence with Raman analysis, the LIG resulting from L1.0 films exhibited at least 2-fold lower R_s than that from the other two films and synthetic polymer-/biomass-based precursors previously reported (Table S1, ESI†), with the lowest R_s (4.5 Ω sq^{-1}) being observed with 30% power level (P30) (Fig. S1f, ESI†). In addition to the optimal laser power, defocused lasing appeared to favor LIG formation compared to focused lasing. Fig. S2 (ESI†) depicts the effects of laser scribing as a function of *z*-axis defocus when the 30% power level was applied. With the *z*-axis defocus distance increased from 0 (on the focal plane) to 2 mm, the I_G/I_D and I_{2D}/I_G ratios reached the highest values for L1.0 (Fig. S2e, ESI†). A further increase in the defocus distance to 3 mm led to comprised LIG quality regardless of the lignin loading in the films.

The LIG resulting from L1.0P30 was further examined for the ultrastructure given its impressive Raman spectrum and low Rs. HRTEM images showed fringe-like patterns of LIG with a *d*-spacing of 0.355 nm between two neighboring (002) planes in graphitic carbon (Fig. 2(d)). This evidence further supported the presence of graphene and suggested the few-layer graphene domain randomly oriented in LIG. The XRD pattern showed characteristic peaks centering at 2θ = 25.9° (assigned to the (002) reflection) and 2θ = 42.9° (assigned to the (100) reflection) (Fig. 2(b)), with an interlayer spacing of 0.344 nm, indicating that L1.0P30 was well graphitized with high crystallinity. Overall, well-identified graphene domains in L1.0P30 proved the successful transformation of lignin into graphene.

3.2. Characterization of LIG/Dragon Skin™ composites

L1.0P30 was selected for the fabrication of strain sensors by transferring LIG to Dragon Skin™. The LIG transfer was assisted

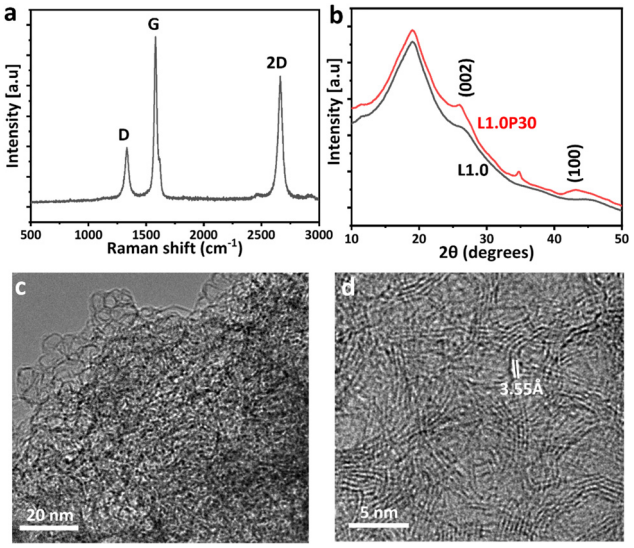

Fig. 2 Characteristics of LIG (L1.0P30). (a) Raman spectrum. (b) XRD spectra of LIG and the pristine film (L.0). (c) and (d) TEM images: scale bars of 20 and 5 nm, respectively.

by spin coating followed by water lifting. Specially, after immersing the whole piece of the Dragon Skin™ spin-coated film in water for about 10 min, the uncarbonized lignin film was automatically detached from LIG. No residual LIG was found in either the detached lignin film or water, while the transferred LIG showed a well retained hierarchical microstructure onto Dragon Skin™ as discussed below. The LIG before and after the transfer was characterized and compared. SEM images show that rigid and clear lines were formed orderly along with traces of CO_2 laser on the surface of pre-transferred LIG (Fig. 3(a) and Fig. S3a, e, ESI†). At higher magnification, LIG showed a foam-like microstructure as typically observed with the LIG synthesis from other precursors (Fig. 3(d) and Fig. S3, ESI†). The porous structure resulted from the rapid release of gaseous molecules (CO_2, H_2O, *etc.*) as byproducts generated from the laser-assisted oxidation and decomposition of the lignin film. Water lifting enabled the facile transfer of LIG without the noticeable loss of LIG. The cross-sectional SEM images also suggested the complete transfer of the LIG layer onto Dragon Skin™ with a similar thickness (115 μm) before and after the transfer (Fig. 3(c) and (f)) and the total thickness of the LIG/Dragon Skin™ composite of ~150 μm. Moreover, this finding suggested sufficient infiltration and curing of Dragon Skin™ into the interconnected network of LIG. Overall, the water lifting method can overcome common issues associated with the LIG transfer onto an elastomeric substrate, such as carbon loss and disruption of the microstructure. As a result, LIG/Dragon Skin™ can well preserve the intrinsic functional properties of LIG and exhibit excellent sensing capability as discussed below.

3.3. Sensing strains and vibrations

The fabricated strain sensors were evaluated for sensitivity in response to two external stimuli, *i.e.*, strains and vibrations. Like many LIG-based strain sensors, the working mechanism of the proposed strain sensor is proposed to be resistance change caused by increasing the gap distance while applying strains. Strikingly, the strain sensor demonstrated ultrasensitivity compared to those based on PI-derived LIG and many other materials (Table S2, ESI†). For example, the gauge factors of strain sensors based on pristine PI-derived LIG reached only up to 160, about 17% of the maximum value given by the proposed strain sensor.[12,15,36] The R_0 of the strain sensor was around 300 Ω, which made it suitable for low power applications. Fig. 4(a) depicts that the sensor experienced three stages

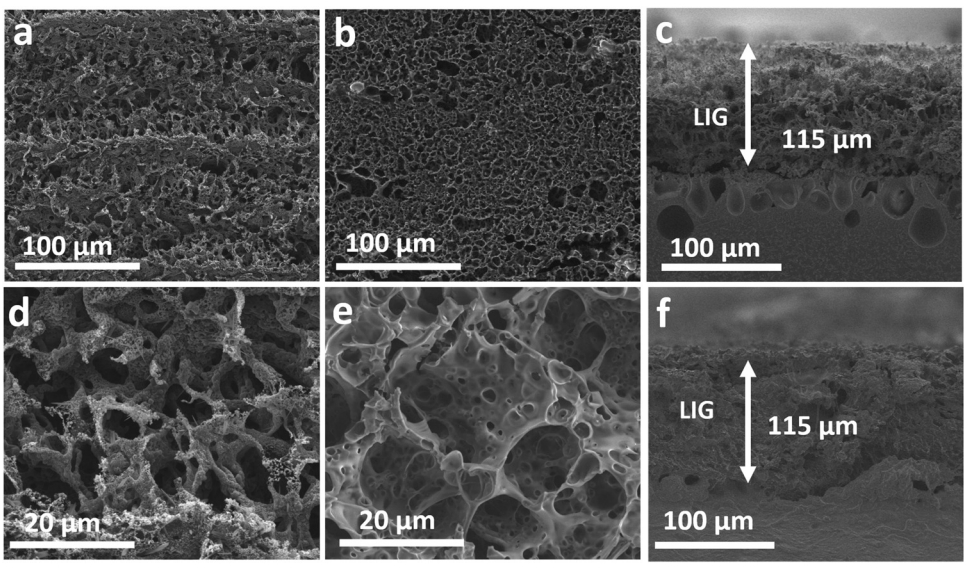

Fig. 3 SEM images of L1.0P30 before and after transfer. (a) and (d) Top view before transfer: scale bars of 100 and 20 μm, respectively. (b) and (e) Top view after transfer: scale bars of 100 and 20 μm, respectively. (c) and (f) Cross-sectional view before transfer and after transfer, respectively: scale bar of 100 μm.

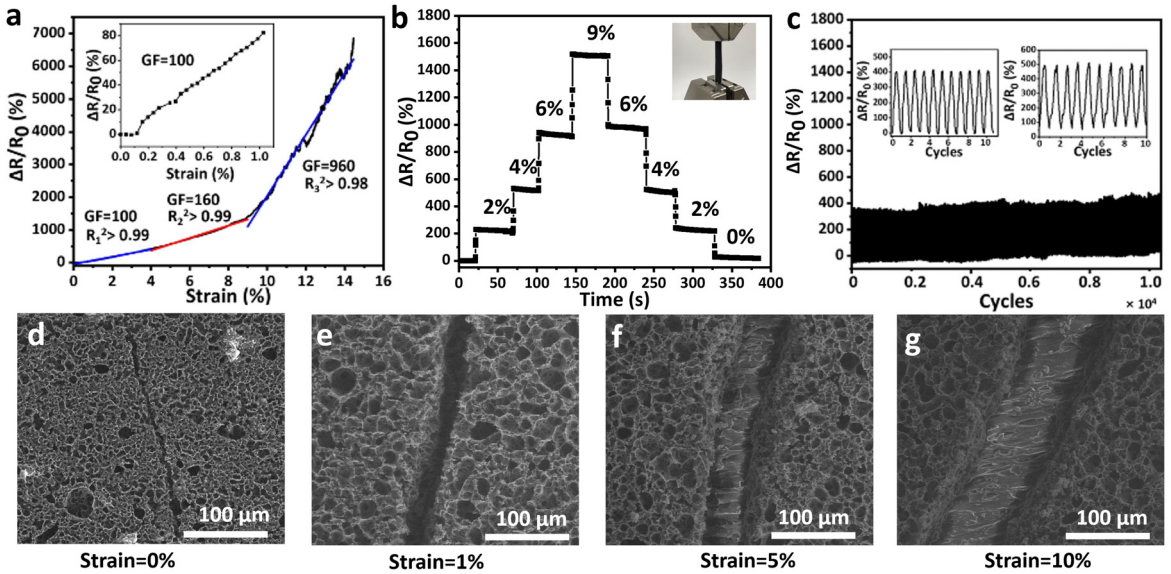

Fig. 4 Sensitivity of the strain sensor to strain. (a) $\Delta R/R_0$ in response to up to 14% strain, with the inset demonstrating the signal change at a stain up to 1%. (b) $\Delta R/R_0$ over the course of testing at different strain levels, with the inset showing the photograph of strain sensor stretching. (c) Sensing stability at 4% strain over 10 000 cycles, with the inset showing the first and last 10 cycles (left and right). (d)–(g) SEM images of the evolution of microgap with an increase in strain: scale bar of 100 μm.

throughout the stretching and the photograph in Fig. 4(b) shows how the sensor was stretched vertically. Its gauge factor was initially about 100 when the strain was below 4%. The sensor also showed good sensitivity even when a strain was applied as low as 0.1% (Fig. S4a, ESI†). The gauge factor became 160 when the strain was increased from 4% to 9%. When the sensor was stretched further from 9% to 14%, the sensor exhibited an excellent gauge factor of ~960. Notably, the signals at three stages had a good linearity, *i.e.*, $R^2 > 99$ for Stages 1 and 2 and $R^2 > 98$ for Stage 3. The sensor was also tested for reversibility in a stretch–release cycle for the hysteresis test. It showed a low degree of hysteresis (<7%) at 9% strain, suggesting good reversibility (Fig. S4b, ESI†). Compared to the strain sensor based on conventional piezoresistive materials such as CNTs and nanowires, LIG-based strain sensors showed a much lower hysteresis degree (Table S2, ESI†).

With the strain range below 9%, the two responding stages can be explained by the fact that with larger strains being applied, the crack between graphene flakes would keep expanding and change into a new junction consisting of reduced conductive paths, leading to the increased gauge factor. The evolution of the crack structure in LIG at different strains applied is also shown in Fig. 4(d)–(g). Within the strain range of 9–14%, the gauge factor was remarkably increased due to the more enlarged cracks. However, when the crack was too large, the electrical connection between responding stages tended to be broken along with more irregular signals, with the maximum strain being applied at 14%. The stability of the signal was tested by applying different strains (*i.e.*, 2%, 4%, 6%, and 9%) (Fig. 4(b)). For each applied strain, the device kept being stretched for 50 s. It was found that the signals of the relative resistance change ($\Delta R/R_0$) were stable and repeatable at a given strain. Compared to start-of-art strain sensors especially based on LIG (Table S2, ESI†), the proposed strain sensor exhibited a significantly improved gauge factor (as high as 960) and markedly lower detection limits (as low as 0.1%) for small-scale strain detections (Fig. S4a, ESI†). Considering excellent sensing linearity, it would be interesting to test and compare with other device configurations like sandwiched structures for ultrasensitivity.[18,19] The sensor was further evaluated for stability over 10 000 stretch–release cycles at 4% strain. There were no significant signal fluctuations being observed after 10 000 cycles (Fig. 4(c)). The resistance of the sensor only increased from around 300 to 450 Ω along with ~10% increase in the gauge factor. The findings demonstrated the excellent stability of the strain sensor's conductive network and reliability for repeated uses, which was shown to be superior to most start-of-art strain sensors fabricated from PI-derived LIG and CNTs (Table S2, ESI†).

In addition to strain sensing, the sensor was also shown to be ultrasensitive to vibration, another form of tiny deformation. The resistance change of the strain sensor was continuously monitored throughout the vibration. Fig. 5(a) and (b) show the resistance in response to a frequency ranging from 5 to 135 Hz with an increment of 5 Hz when the input voltage was kept at 2 V. $\Delta R/R_0$ first increased along with the increasing frequency until reaching the highest value at 80 Hz. When the frequency was increased further, $\Delta R/R_0$ drastically decreased to 35% at 100 Hz and then increased. The spike in $\Delta R/R_0$ at 80 Hz suggested that this frequency could be at or near the resonant frequency/natural frequency of the sensor. As a result, the sensor can vibrate with a larger amplitude than that at non-resonant frequencies. The larger vibration amplitude can

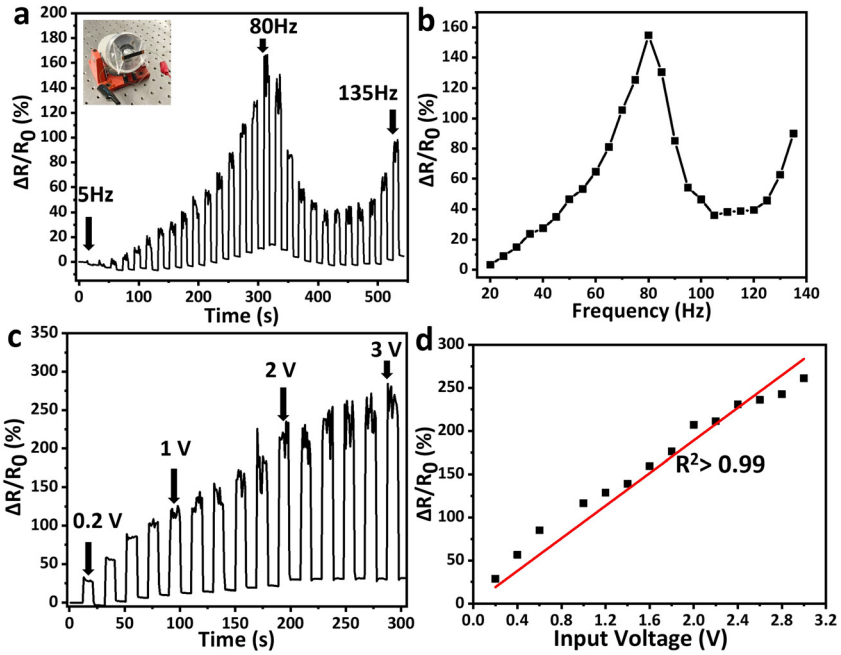

Fig. 5 Sensitivity of the strain sensor to vibration. (a) $\Delta R/R_0$ at different vibration frequencies (5–135 Hz) when the input voltage for the vibration was applied at 2 V. (b) Averaged $\Delta R/R_0$ at different frequencies (5–135 Hz). (c) $\Delta R/R_0$ at different input voltages (0.2–3 V) for the vibration when a vibration frequency was applied at 80 Hz. (d) Linear correlation between $\Delta R/R_0$ and input voltages. The photograph in (a) shows the testing setup in which the sensor was attached to a permanent magnetic electrodynamic shaker to which an input voltage was provided.

lead to larger cracks and subsequently more significant signal changes. The electrical resistance of the sensor was further measured against the amplitude range controlled by input voltages from 0.2 to 3 V when applying a frequency of 80 Hz (Fig. 5(c)). An excellent linear correlation between $\Delta R/R_0$ and input voltage was observed ($R^2 > 99$) (Fig. 5(d)). These results indicate that lignin derived LIG has exceptional piezoresistive properties that can also be explored for sound-related applications.

3.4. Sensors for detecting speaking

The sensor was used as a speaking detector given the frequency of human speaking ranging from 50 to 300 Hz. Fig. 6 and Fig. S5 (ESI†) depicts the representative performance of the strain on detecting human speaking by sensing throat muscle movements and vibrations (Fig. S5a, ESI†). Swallow, one of the typical muscle movements, was also detected, showing distinguishing patterns (Fig. 6(a)). When one was asked to speak two example words "today" and "beautiful" and the whole sentence

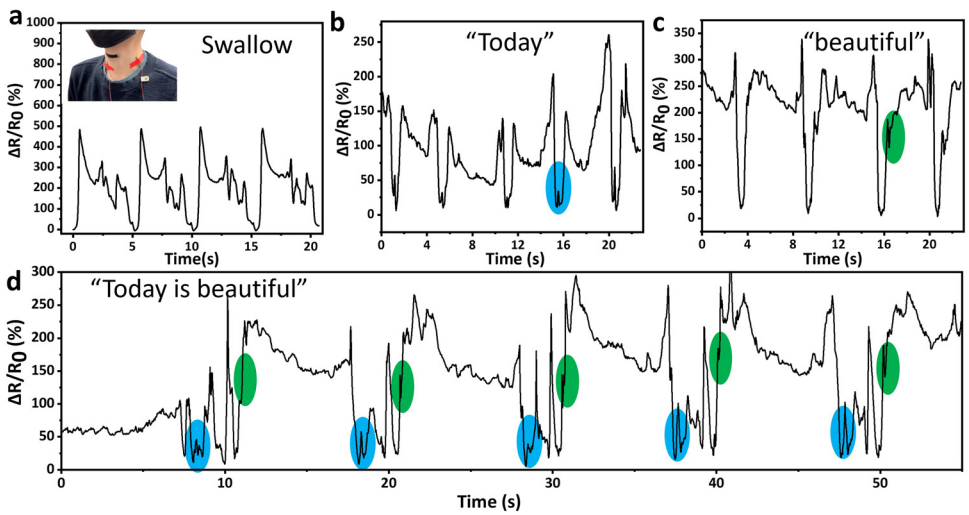

Fig. 6 Strain sensor working as a speaking detector. (a) $\Delta R/R_0$ of detecting swallow. (b)–(d) $\Delta R/R_0$ of detecting speaking "beautiful," "today," and "today is beautiful", respectively. The blue and green ovals in (b)–(d) represent signature peaks of the signals during one's speaking "today" and "beautiful" which were well identified in the whole sentence. The photograph in (a) shows the placement of the sensor for detecting swallowing and speaking.

"Today is beautiful" 4–5 times, the signature peaks corresponding to two individual words were well identified in the whole sentence (Fig. 6(b)–(d)). More intriguingly, when the speaking testing was extended to a longer sentence "Laser-induced graphene from lignin-based precursor has many good properties." three times, the signature patterns of individual words were clearly detected, with good repeatability (Fig. S5b–m and S7a, ESI†). These findings suggested that the sensor can distinguish tiny deformations caused by speaking, with reliable and repeatable performance. The sensing mechanism for speaking is a combined effect of strains and vibrations. On one hand, the muscle movements of the throat during speaking are unique and repeatable, which can be captured as a strain stimulus by the sensor. On the other hand, sound generated during speaking causes vibrations to the sensor. The exceptional sensitivity of the sensor to strains, vibrations, or combined suggests its great potential to be used as a sophisticated speaking detector. One example would be aiding people with disability in speaking by coupling artificial intelligence.

3.5. Sensor for small-scale human motion detection

The performance of the sensor in detecting human motions, including eyeball movements, heartbeats (pulses), breath, and seismocardiography (SCG), is depicted in Fig. 7. The sensor showed excellent and stable responses. For eyeball movements, the sensor was horizontally attached to the lower part of one's eyes for eye blinks, fast eye blinks, looking up, looking down, looking left, and looking right in order, each three times except fast eye blinks. Fig. 7(a) shows that the strain sensor can provide instant and clear feedback with the unique, stable, and repeatable resistance change patterns for different eye movements. Muscle movements controlling an eyeball to different directions were at tiny scales. Compared to the reported eyeball movement sensors.[37,38] the proposed strain sensor offers a simpler way to monitor the real-time eye movement detection for human health monitoring and virtual reality system.[38,39] Furthermore, the strain sensor was attached to one's chest for breath detection, including belly breath (deep breath) and chest breath (normal breath) (Fig. 7(b)). As breath disorder is usually related to pulmonary diseases (asthma, COVID-19, *etc.*), the ability of the strain sensor to distinguish breath patterns would be highly useful for respiratory system monitoring.

SCG is a non-invasive technique used for cardiovascular disease diagnosis by measuring vibrations around the chest caused by one's heartbeats. The strain sensor was also evaluated for its performance in the SCG signal recording. Fig. 7(c) depicts the signal patterns to body microvibrations during one cycle of holding breath including the systole phase and diastole phase. The corresponding region of the signal for two phases and their related heart activities are shown in the inset of Fig. 7(c). Specifically, mitral valve closure (MC), aortic valve opening (AO), and rapid blood ejection (RE) from the systole phase and aortic valve closure (AC), mitral valve opening (MO), and rapid blood filling (RF) from the diastole phase are annotated. The SCG acquired from different positions around the chest including its low part was distinguishing given different structures of the human body (Fig. 7(c) and Fig. S6, ESI†). The signals showed good repeatability across all the

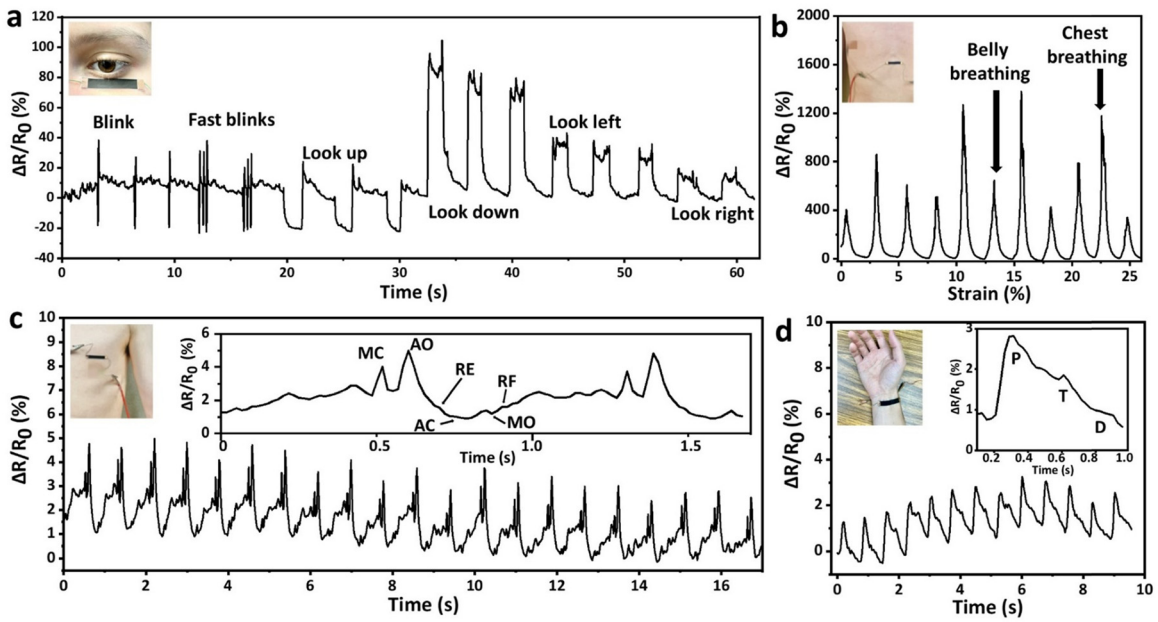

Fig. 7 Strain sensor for human motion monitoring. (a) Signal patterns of monitoring eyeball movements. (b) Signal patterns of monitoring belly and chest breath. (c) Signal patterns of SCG. (d) Signal patterns of pulses. The photographs show the placement of the sensor at different positions for testing. The inset in (c) annotates mitral valve closure (MC), aortic valve opening (AO), and rapid blood ejection (RE) from the systole phase and aortic valve closure (AC), mitral valve opening (MO), and rapid blood filling (RF) from the diastole phase. The inset in (d) shows the signal changes caused by the percussion wave (P), tidal wave (T), and diastolic wave (D).

testing cycles based on an error band analysis (Fig. S7b, ESI†). Although the relationship between SCG and electrocardiogram (ECG) is not well understood, recent advances, including more accessible sensors and better algorithms enhanced by machine learning, have demonstrated the potential of SCG in monitoring the health of the patient with heart diseases.[40] The proposed strain sensor, which can be facilely fabricated from lignin derived LIG at low cost, can serve the purpose for easy and rapid SCG detection.

Pulse wave detection is another key parameter in human health monitoring. As shown in Fig. 7(d), the sensor can distinguish the deformations caused by the percussion wave (*P*), tidal wave (*T*), and diastolic wave (*D*), which are important indicators of one's cardiovascular health monitoring.[41]

4. Conclusions

The lignin-derived strain sensor had excellent performance in the detection of small deformations caused by strains and vibrations. It exhibited a large working range for sensing up to 14% strain, with a gauge factor as high as 960 and low hysteresis. A good linear relationship between the relative resistance changes and strains was observed. It was also sensitive to vibrations in response to changes in frequencies and amplitudes. Moreover, the strain sensor can capture tiny deformations based on human speaking, eyeball movements, breath, seismocardiography, and pulses. In all the tests, the strain sensor showed excellent stability and repeatability and was able to generate distinguishing signal patterns of deformations caused by various external stimuli. This work indicated that LIG induced from lignin can be used as an excellent piezoresistive material to fabricate wearable, high-performance, ultrasensitive strain sensors for the detection of strain-/vibration-induced deformations toward applications such as healthcare monitoring and sound sensing.

Conflicts of interest

There are no conflicts to declare.

Acknowledgements

This work was supported by the National Science Foundation (Award No. 1933861). The authors thank Domtar Corporation (Fort Mills, South Carolina) for providing kraft lignin.

References

1 Y. Wang, L. Wang, T. T. Yang, X. Li, X. B. Zang, M. Zhu, K. L. Wang, D. H. Wu and H. W. Zhu, Wearable and highly sensitive graphene strain sensors for human motion monitoring, *Adv. Funct. Mater.*, 2014, **24**(29), 4666–4670.

2 D. Son, J. Lee, S. Qiao, R. Ghaffari, J. Kim, J. E. Lee, C. Song, S. J. Kim, D. J. Lee, S. W. Jun, S. Yang, M. Park, J. Shin, K. Do, M. Lee, K. Kang, C. S. Hwang, N. S. Lu, T. Hyeon and D. H. Kim, Multifunctional wearable devices for diagnosis and therapy of movement disorders, *Nat. Nanotechnol.*, 2014, **9**(5), 397–404.

3 C. Pang, J. H. Koo, A. Nguyen, J. M. Caves, M. G. Kim, A. Chortos, K. Kim, P. J. Wang, J. B. H. Tok and Z. A. Bao, Highly skin-conformal microhairy sensor for pulse signal amplification, *Adv. Mater.*, 2015, **27**(4), 634–640.

4 C. Y. Yan, J. X. Wang, W. B. Kang, M. Q. Cui, X. Wang, C. Y. Foo, K. J. Chee and P. S. Lee, Highly stretchable piezoresistive graphene-nanocellulose nanopaper for strain sensors, *Adv. Mater.*, 2014, **26**(13), 2022–2027.

5 Z. X. Wu, W. X. Shi, H. J. Ding, B. Z. Zhong, W. X. Huang, Y. B. Zhou, X. C. Gui, X. Xie and J. Wu, Ultrastable, stretchable, highly conductive and transparent hydrogels enabled by salt-percolation for high-performance temperature and strain sensing, *J. Mater. Chem. C*, 2021, **9**(39), 13668–13679.

6 L. Huang, S. Xu, Z. Wang, K. Xue, J. Su, Y. Song, S. Chen, C. Zhu, B. Z. Tang and R. Ye, Self-reporting and photothermally enhanced rapid bacterial killing on a laser-induced graphene mask, *ACS Nano*, 2020, **14**(9), 12045–12053.

7 S. Park, M. Vosguerichian and Z. A. Bao, A review of fabrication and applications of carbon nanotube film-based flexible electronics, *Nanoscale*, 2013, **5**(5), 1727–1752.

8 T. Yamada, Y. Hayamizu, Y. Yamamoto, Y. Yomogida, A. Izadi-Najafabadi, D. N. Futaba and K. Hata, A stretchable carbon nanotube strain sensor for human-motion detection, *Nat. Nanotechnol.*, 2011, **6**(5), 296–301.

9 S. R. Pan, Z. Pei, Z. Jing, J. Q. Song, W. D. Zhang, Q. Zhang and S. B. Sang, A highly stretchable strain sensor based on CNT/graphene/fullerene-SEBS, *RSC Adv.*, 2020, **10**(19), 11225–11232.

10 S. Chen, Y. Wei, X. Yuan, Y. Lin and L. Liu, A highly stretchable strain sensor based on a graphene/silver nanoparticle synergic conductive network and a sandwich structure, *J. Mater. Chem. C*, 2016, **4**(19), 4304–4311.

11 X. Li, R. J. Zhang, W. J. Yu, K. L. Wang, J. Q. Wei, D. H. Wu, A. Y. Cao, Z. H. Li, Y. Cheng, Q. S. Zheng, R. S. Ruoff and H. W. Zhu, Stretchable and highly sensitive graphene-on-polymer strain sensors, *Sci. Rep.*, 2012, **2**, 870.

12 A. F. Carvalho, A. J. S. Fernandes, C. Leitão, J. Deuermeier, A. C. Marques, R. Martins, E. Fortunato and F. M. Costa, Laser-induced graphene strain sensors produced by ultraviolet irradiation of polyimide, *Adv. Funct. Mater.*, 2018, **28**(52), 1805271.

13 A. Dallinger, K. Keller, H. Fitzek and F. Greco, Stretchable and skin-conformable conductors based on polyurethane/laser-induced graphene, *ACS Appl. Mater. Interfaces*, 2020, **12**(17), 19855–19865.

14 S. Y. Jeong, J. U. Lee, S. M. Hong, C. W. Lee, S. H. Hwang, S. C. Cho and B. S. Shin, Highly skin-conformal laser-induced graphene-based human motion monitoring sensor, *Nanomaterials*, 2021, **11**(4), 951.

15 S. Y. Jeong, Y. W. Ma, J. U. Lee, G. J. Je and B. S. Shin, Flexible and highly sensitive strain sensor based on laser-induced graphene pattern fabricated by 355 nm pulsed laser, *Sensors*, 2019, **19**(22), 4867.

16 L. Q. Tao, H. Tian, Y. Liu, Z. Y. Ju, Y. Pang, Y. Q. Chen, D. Y. Wang, X. G. Tian, J. C. Yan, N. Q. Deng, Y. Yang and T. L. Ren, An intelligent artificial throat with sound-sensing ability based on laser induced graphene, *Nat. Commun.*, 2017, **8**, 14579.

17 H. Wang, Z. F. Zhao, P. P. Liu and X. G. Guo, Laser-induced porous graphene on polyimide/PDMS composites and its kirigami-inspired strain sensor, *Theor. Appl. Mech. Lett.*, 2021, **11**(2), 100240.

18 M. S. Fan, L. Wu, Y. P. Hu, M. J. Qu, S. T. Yang, P. Tang, L. J. Pan, H. Wang and Y. Z. Bin, A highly stretchable natural rubber/buckypaper/natural rubber (NR/N-BP/NR) sandwich strain sensor with ultrahigh sensitivity, *Adv. Compos. Mater.*, 2021, **4**(4), 1039–1047.

19 C. W. Li, S. T. Yang, Y. Guo, H. Huang, H. Chen, X. Q. Zuo, Z. Fan, H. W. Liang and L. J. Pan, Flexible, multi-functional sensor based on all-carbon sensing medium with low coupling for ultrahigh-performance strain, temperature and humidity sensing, *Chem. Eng. J.*, 2021, **426**, 1385–8947.

20 R. Rahimi, M. Ochoa, W. Y. Yu and B. Ziaie, Highly stretchable and sensitive unidirectional strain sensor via laser carbonization, *ACS Appl. Mater. Interfaces*, 2015, **7**(8), 4463–4470.

21 J. J. Park, W. J. Hyun, S. C. Mun, Y. T. Park and O. O. Park, Highly stretchable and wearable graphene strain sensors with controllable sensitivity for human motion monitoring, *ACS Appl. Mater. Interfaces*, 2015, **7**(11), 6317–6324.

22 Y. Wang, T. T. Yang, J. C. Lao, R. J. Zhang, Y. Y. Zhang, M. Zhu, X. Li, X. B. Zang, K. L. Wang, W. J. Yu, H. Jin, L. Wang and H. W. Zhu, Ultra-sensitive graphene strain sensor for sound signal acquisition and recognition, *Nano Res.*, 2015, **8**(5), 1627–1636.

23 L. X. Huang, H. Wang, P. X. Wu, W. M. Huang, W. Gao, F. Y. Fang, N. Cai, R. X. Chen and Z. M. Zhu, Wearable flexible strain sensor based on three-dimensional wavy laser-induced graphene and silicone rubber, *Sensors*, 2020, **20**(15), 4266.

24 S. D. Luo, P. T. Hoang and T. Liu, Direct laser writing for creating porous graphitic structures and their use for flexible and highly sensitive sensor and sensor arrays, *Carbon*, 2016, **96**, 522–531.

25 B. Kulyk, B. F. R. Silva, A. F. Carvalho, S. Silvestre, A. J. S. Fernandes, R. Martins, E. Fortunato and F. M. Costa, Laser-induced graphene from paper for mechanical sensing, *ACS Appl. Mater. Interfaces*, 2021, **13**(8), 10210–10221.

26 R. Ye, Y. Chyan, J. Zhang, Y. Li, X. Han, C. Kittrell and J. M. Tour, Laser-induced graphene formation on wood, *Adv. Mater.*, 2017, **29**(37), 170221.

27 Y. Chyan, R. Q. Ye, Y. L. Li, S. P. Singh, C. J. Arnusch and J. M. Tour, Laser-induced graphene by multiple lasing: Toward electronics on cloth, paper, and food, *ACS Nano*, 2018, **12**(3), 2176–2183.

28 W. L. Zhang, Y. J. Lei, F. W. Ming, Q. Jiang, P. M. F. J. Costa and H. N. Alshareef, Lignin laser lithography: A direct-write method for fabricating 3D graphene electrodes for micro-supercapacitors, *Adv. Energy Mater.*, 2018, **8**(27), 1801840.

29 J. Lin, Z. Peng, Y. Liu, F. Ruiz-Zepeda, R. Ye, E. L. Samuel, M. J. Yacaman, B. I. Yakobson and J. M. Tour, Laser-induced porous graphene films from commercial polymers, *Nat. Commun.*, 2014, **5**, 5714.

30 A. J. Ragauskas, G. T. Beckham, M. J. Biddy, R. Chandra, F. Chen, M. F. Davis, B. H. Davison, R. A. Dixon, P. Gilna, M. Keller, P. Langan, A. K. Naskar, J. N. Saddler, T. J. Tschaplinski, G. A. Tuskan and C. E. Wyman, Lignin valorization: Improving lignin processing in the biorefinery, *Science*, 2014, **344**(6185), 709–720.

31 F. Mahmood, H. Zhang, J. Lin and C. Wan, Laser-induced graphene derived from kraft lignin for flexible supercapacitors, *ACS Omega*, 2020, **5**(24), 14611–14618.

32 F. Mahmood, C. Zhang, Y. C. Xie, D. Stalla, J. Lin and C. X. Wan, Transforming lignin into porous graphene via direct laser writing for solid-state supercapacitors, *RSC Adv.*, 2019, **9**, 22713–22720.

33 F. Mahmood, Y. Sun and C. X. Wan, Biomass-derived porous graphene for electrochemical sensing of dopamine, *RSC Adv.*, 2021, **11**, 15410–15415.

34 C. W. Lee, S. Y. Jeong, Y. W. Kwon, J. U. Lee, S. C. Cho and B. S. Shin, Fabrication of laser-induced graphene-based multifunctional sensing platform for sweat ion and human motion monitoring, *Sens. Actuators, A*, 2022, **334**, 113320.

35 A. C. Ferrari, J. C. Meyer, V. Scardaci, C. Casiraghi, M. Lazzeri, F. Mauri, S. Piscanec, D. Jiang, K. S. Novoselov, S. Roth and A. K. Geim, Raman spectrum of graphene and graphene layers, *Phys. Rev. Lett.*, 2006, **97**(18), 187401.

36 T. Han, A. Nag, R. B. V. B. Simorangkir, N. Afsarimanesh, H. R. Liu, S. C. Mukhopadhyay, Y. Z. Xu, M. Zhadobov and R. Sauleau, Multifunctional flexible sensor based on laser-induced graphene, *Sensors*, 2019, **19**, 3477.

37 S. Mishra, Y. S. Kim, J. Intarasirisawat, Y. T. Kwon, Y. Lee, M. Mahmood, H. R. Lim, R. Herbert, K. J. Yu, C. S. Ang and W. H. Yeo, Soft, wireless periocular wearable electronics for real-time detection of eye vergence in a virtual reality toward mobile eye therapies, *Sci. Adv.*, 2020, **6**(11), 1729.

38 A. Al-Rahayfeh and M. Faezipour, Eye tracking and head movement detection: A state-of-art survey, *IEEE J. Transl. Eng. Health Med.*, 2013, **1**, 2100212.

39 T. T. Brunye, T. Drew, D. L. Weaver and J. G. Elmore, A review of eye tracking for understanding and improving diagnostic interpretation, *CRPI Implic.*, 2019, **4**, 7.

40 A. Taebi, B. E. Solar, A. J. Bomar, R. H. Sandler and H. A. Mansy, Recent advances in seismocardiography, *Vibration*, 2019, **2**(1), 64–86.

41 T. T. Yang, X. Jiang, Y. J. Zhong, X. L. Zhao, S. Y. Lin, J. Li, X. M. Li, J. L. Xu, Z. H. Li and H. W. Zhu, A wearable and highly sensitive graphene strain sensor for precise home-based pulse wave monitoring, *ACS Sens.*, 2017, **2**(7), 967–974.

